Article

Journal of
Nanoscience and Nanotechnology
Vol. 17, 1650–1656, 2017
www.aspbs.com/jnn

Effects of Rapid Solidification on Phase Formation and Microstructure Evolution of $AgSbTe_2$-Based Thermoelectric Compounds

Alberto Castellero[1,*], Gianluca Fiore[1], Eliran Evenstein[2], Marcello Baricco[1], and Yaron Amouyal[2]

[1] *Department of Chemistry and NIS, University of Turin, via P. Giuria 7, 10125 Torino, Italy*
[2] *Department of Materials Science and Engineering, Technion – Israel Institute of Technology, 32000 Haifa, Israel*

We report on rapid solidification of an $Ag_{16.7}Sb_{30.0}Te_{53.3}$ compound using planar flow casting to stabilize the δ-$AgSbTe_2$ single phase and avoid precipitation of the interconnected Sb_2Te_3 phase, which leads to deterioration of thermoelectric properties. Rapidly solidified samples are in form of flakes with different thickness (60–400 μm). Precipitation of Sb_2Te_3 phase is fully inhibited in thin flakes (thickness below 100 μm), which consist of an homogeneous δ-$AgSbTe_2$ matrix, whereas isolated Sb_2Te_3 precipitates, dispersed throughout the δ-$AgSbTe_2$ matrix, were found in thick flakes (thickness above 100 μm). The lattice parameter of the δ-$AgSbTe_2$ phase progressively increases with the cooling rate, indicating progressive supersaturation of the matrix for high degree of supercooling. Bulk specimens were prepared by hot pressing of the rapidly solidified flakes to evaluate thermoelectric properties. After sintering of the rapidly solidified flakes, the differential scanning calorimetry (DSC) traces indicates partial decomposition of the non equilibrium δ-$AgSbTe_2$ into the stable phases. Measurements of the thermoelectric transport properties indicate the positive effects of rapid solidification on thermal conductivity and Seebeck coefficient and its negative effect on electrical conductivity, suggesting an operative way to improve thermoelectric performance.

Keywords: Rapid Solidification, $AgSbTe_2$, Thermoelectric Materials, Metastable Phases, Thermoelectric Transport Properties.

1. INTRODUCTION

$AgSbTe_2$-based compounds attract interest from both experimental and computational points of view[1] owing to their good thermoelectric (TE) properties in the medium temperature range,[2] and since they are constituents of the high performance lead-antimony-silver-telluride (*LAST*) alloys.[3] The δ-phase of the Ag–Sb–Te system, which is a Sb-rich off-stoichiometric $AgSbTe_2$ compound, exists over a certain composition range of $Ag_{0.672}Sb_{1.116-1.38}Te_2$, as recently confirmed by Nielsen et al.[4] Upon cooling, the δ-phase decomposes at 360 °C into the Ag_2Te and Sb_2Te_3 phases via an eutectoid reaction.[5] However, this eutectoid reaction is kinetically hindered,[6] so that metastable δ-phase can be retained below 360 °C. Upon heating, the metastable δ-phase slowly starts to decompose into the stable phases at around 300 °C, as shown by *in-situ* X-ray diffraction experiments.[7] Metastable single δ-phase can be obtained upon cooling only by non-equilibrium techniques, such as water quenching[8] and melt spinning.[9] Slow cooling allows the solid state precipitation of Sb_2Te_3 above 360 °C due to crossing of the solvus. From the TE properties point of view, δ-phase is characterized by an extremely low value of thermal conductivity (around 0.7 $Wm^{-1}K^{-1}$) due to phonon mean path that is limited to interatomic distances.[10] This behavior has been related to an intrinsic nanostructure originating from the ordering of cations into nanoscale domains (about 3 nm).[11] TE properties of δ-$AgSbTe_2$ are affected by the presence of second phases (i.e., Sb_2Te_3 or Ag_2Te)[12–15] and lattice defects,[16] which are manifested by either boundary scattering or two-phase rule-of-mixture.

In the case of Sb_2Te_3 precipitates, heterogeneous nucleation of the second phase occurs on planar defects and grain boundaries of the δ-$AgSbTe_2$ host phase, leading to the formation of coarse Widmanstätten microstructure with interconnected lamellar Sb_2Te_3 precipitates dispersed in

*Author to whom correspondence should be addressed.

 1533-4880/2017/17/1650/007 doi:10.1166/jnn.2017.13736

the δ-$AgSbTe_2$ matrix along specific lattice directions.[8, 17] On the one hand, such microstructure favors parallel conduction, hindering heat and charge carriers from crossing interfaces. Thus, electrical and thermal conductivities do not significantly change as a function of the volume fraction of Sb_2Te_3 precipitates. On the other hand, the Seebeck coefficient of the Sb_2Te_3/δ-$AgSbTe_2$ composite decreases when increasing volume fraction of Sb_2Te_3 precipitates, because of the effective medium behavior.[8]

In the case of Ag_2Te precipitates, dispersion of nanometer-size second phase in the δ-$AgSbTe_2$ matrix was reported.[14, 18] In such nanostructured two-phase systems, charge and heat carriers are effectively scattered at the interfaces, as shown by the concomitant decrease of the electrical and thermal conductivities, with respect to the single phase state.[14, 18] Furthermore, precipitation of Ag_2Te leads to the increase of the Seebeck coefficient, which was explained invoking the carrier's energy filtering effect.[14, 18] However, the applicability of the Ag_2Te/δ-$AgSbTe_2$ system is questionable due to the occurrence of a phase transition between monoclinic and cubic Ag_2Te at about 144 °C,[4] which lays inside the working temperature range of the material. The effect of this reversible phase transition on the performance of the device needs to be investigated further.

Formation of a fully-supersaturated single δ-$AgSbTe_2$ matrix is very important for studying the microstructure evolved upon aging heat treatments, yet this is not an easy task thanks to the relatively fast nucleation rate of Sb_2Te_3. Rapid solidification methods can well-address this issue. In this work, rapidly solidified δ-$AgSbTe_2$ samples were prepared using planar-flow casting, which allows to reach cooling rates between 10^4 and 10^5 °C/s,[19] with the aim to study the dependence of phase formation and microstructure evolution on cooling conditions. Thermoelectric properties were evaluated on sintered pellets obtained by hot pressing of the rapidly solidified samples and compared with respect to reference samples.[1]

2. EXPERIMENTAL PROCEDURE

A master alloy of composition $Ag_{16.7}Sb_{30}Te_{53.3}$ (at. %) was prepared by melting of elemental Ag, Sb and Te (99.99 at. % purity) in an evacuated ($<10^{-5}$ torr) and sealed quartz ampoule that was refilled with a mixture of Ar-7 vol.% H_2at 850 °C for 2 h. The melt was quenched in an iced-water bath.[1] Rapidly solidified samples were prepared using a planar flow casting apparatus (Edmund Bühler GmbH) in Ar atmosphere (1 bar). The master alloy was induction melted in a BN crucible and ejected by an Ar overpressure (0.2 bar) on a copper wheel rotating at 40 m/s. As a consequence of the extreme brittleness of the alloy, formation of continuous ribbons is limited and fragmented flakes with different thickness (ranging from 60 μm to 400 μm) form during rapid solidification. The rapidly solidified samples were classified as thin (thickness less than 100 μm) and thick (thickness larger than 100 μm) flakes.

In addition to the above-detailed procedure, we produced reference specimens by annealing an ampoule containing the same master alloy at 850 °C (in the liquid phase) for 2 h and moderate cooling down to 600 °C with 2 h dwell, followed by slow cooling (−5 K/min) to 556 °C and homogenization for 80 h. Then, the alloy was quenched in an iced-water bath. In this way, we aim to evaluate the effect of the cooling rate on the stabilization of the metastable single δ-phase.

Structural characterization was performed using X-ray diffraction (XRD) analysis. Measurements were performed for powder specimens using a PANalytical X'Pert Pro diffractometer with Bragg-Brentano geometry and Cu–Kα radiation. Lattice parameters of the crystalline phases were determined applying the Rietveld refinement technique[20] using the MAUD software.[21] The degree of preferred crystallographic orientation was estimated through the Lotgering orientation factor, LF, defined as

$$\mathrm{LF} = \frac{p - p_0}{1 - p_0} \tag{1}$$

where p is the ratio between the summation of the diffraction peak intensities corresponding to the preferential orientation and the summation of all the diffraction peak intensities; p_0 is the value of p for a randomly oriented sample.[22] Samples for metallographic analysis were prepared by metallographic polishing with abrasive paste (40 nm) and etching with a solution of HNO_3 (45 vol.%) and distilled water (55 vol.%) for 30 seconds. The microstructure of the samples was observed using a Leica DMLM optical microscope and a Leica Steroscan 410 Scanning Electron Microscope (SEM), equipped with an Oxford Instruments INCAx-sight probe for Energy Dispersive X-ray analysis (EDX), which was used to determine phase composition. EDX analysis was performed on unpolished samples using pure Co as a standard.

Thermal stability of reference samples, as quenched rapidly solidified flakes and sintered rapidly solidified flakes was investigated using a SETARAM 1600 differential scanning calorimeter (DSC) with a scanning rate of 25 K/min.

To test the TE properties of both rapidly-solidified and reference samples, we first produced 3 mm thick and 12.7 mm dia. pellets by milling the raw materials (rapidly solidified samples and water-quenched flakes of the reference material) to fine powder having particle size $<$50–60 μm using mortar and pestle. The powders were then pressed in stainless steel dies at 550 °C for 30 min at protective atmosphere under 25 MPa uniaxial pressure along the normal direction.

The temperature-dependent electrical conductivity, $\sigma(T)$, and Seebeck coefficient (thermopower, $S(T)$), of these pellets were measured at the temperature range of 30 through 400 °C employing the *Nemesis* SBA-458

apparatus (Netzsch GmbH, Selb, Germany), which is designed for simultaneous measurements of electrical conductivity and thermopower for planar geometry.[23–25]

The thermal conductivity values of the pellets, $\kappa(T)$, were determined by measuring their temperature-dependent thermal diffusivity, $\alpha(T)$, and specific heat, $C_p(T)$, as well as the density, ρ; $\kappa(T)$ is then expressed by:[26]

$$\kappa(T) = \alpha(T) \cdot \rho \cdot C_p(T) \quad (2)$$

We utilized a *Microprobe* LFA-457 laser flash analyzer (LFA; Netzsch GmbH, Selb, Germany) to directly measure the thermal diffusivity of the pellets for the same temperature range, with an instrumental accuracy of 2%. The material's densities were measured at room temperature, and their dependence on temperature was neglected. The temperature-dependent heat capacity was simultaneously measured in the LFA in a comparative method using a pure Al_2O_3-reference sample having similar geometry.[23] The resulting accuracy of the evaluation of thermal conductivity values was 10%.

3. RESULTS AND DISCUSSION

We performed EDX chemical composition analysis for the as quenched rapidly solidified samples, and the results indicate that their average composition (reported together with the corresponding standard deviation) is comparable with the nominal one within the sensitivity limit of the technique, as shown in Table I.

We performed XRD analysis for both quenched master alloy and rapidly solidified samples (thick and thin flakes), and the results are displayed in Figure 1. The experimental and calculated values are represented by black dots and red lines, respectively. The presence of δ-$AgSbTe_2$ phase (space group $Fm\bar{3}m$) is indicated for all samples. However, for the master alloy, the peak at 44.6° could not be assigned. The difference between the calculated and the experimental patterns (blue line) suggests the presence of different preferred crystallographic orientations for the samples processed at different conditions, that is, {hh0} and {h00} for the master alloy and the rapidly solidified samples, respectively. The values of the Lotgering factor, reported in Table II, show a slight increase of the preferred orientation degree as the cooling rate increases.

Table II shows the lattice parameters that were evaluated for the cubic ($Fm\bar{3}m$) δ-$AgSbTe_2$ phase in the different

Table I. Average values and standard deviation of the chemical composition, measured by EDX, in the rapidly solidified samples (thick and thin flakes).

	Ag (at.%)	Sb (at.%)	Te (at.%)
Nominal	16.7	30.0	53.3
Rapidly solidified samples (thick and thin flakes)	17.0 ± 0.4	29.2 ± 0.8	53.8 ± 0.5

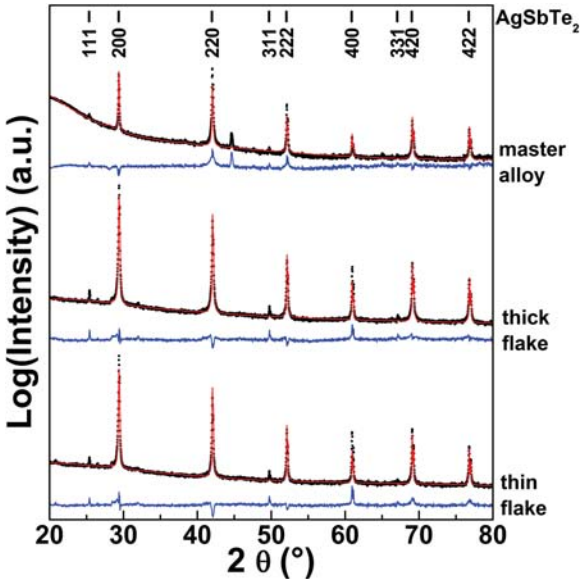

Figure 1. Experimental (black dots) and calculated (red lines) XRD patterns collected from the as-quenched master alloy and rapidly solidified samples (thick and thin flakes). The blue lines represent the difference between experimental and calculated patterns. Vertical lines in the top represent the position of the indexed crystallographic reflections for the δ-$AgSbTe_2$ phase (space group $Fm\bar{3}m$).

samples from Rietveld refinement. It is found that the lattice parameter increases with increasing cooling rate (thin flake > thick flake > master alloy).

Figures 2(a and b) show the optical and SEM (secondary electron detector) micrographs, respectively, of the etched master alloy. The microstructure is characterized by lamellar precipitates, indicated by arrows in Figure 2(b), dispersed in the matrix that, according to previous literature reports,[1,17] can be identified as Sb_2Te_3, although not detected in the XRD pattern shown in Figure 1. The Sb_2Te_3 precipitates and the δ-$AgSbTe_2$ matrix form an interconnected lamellar Widmanstätten microstructure with orientation relationship of $(0001)Sb_2Te_3 \parallel (111)$δ-$AgSbTe_2$, as reported by Medlin et al.[16] A similar microstructure was observed also for the as quenched and sintered reference sample as reported in Ref. [1].

Table II. Lattice parameter of δ-$AgSbTe_2$ in the master alloy and rapidly solidified samples (thick and thin flakes); Lotgering orientation factor for the the master alloy and rapidly solidified samples (thick and thin flakes).

Sample	Phase	Lattice parameter (Å)	Preferred crystallographic orientation	Lotgering factor, LF
Master alloy	δ-$AgSbTe_2$	6.0752	{hh0}	0.12
Rapidly solidified thick flake	δ-$AgSbTe_2$	6.0768	{h00}	0.27
Rapidly solidified thin flake	δ-$AgSbTe_2$	6.0781	{h00}	0.30

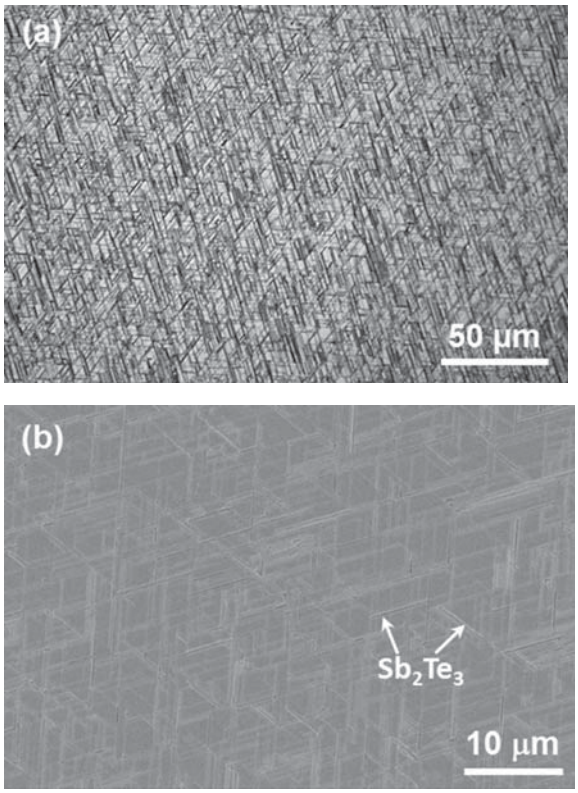

Figure 2. (a) Optical micrograph of the etched surface of the as-quenched master alloy. (b) secondary electron micrograph of the etched surface of the as-quenched master alloy: the arrows indicate the Sb_2Te_3 precipitates.

Figure 3(a) shows a SEM micrograph (5 kV secondary electron signal) of the non-etched cross-section of a thick flake having an average thickness of 130 μm. The microstructure is characterized by columnar grains with a thickness ranging between 10 μm and 30 μm. Figures 3(b and c) show optical and SEM (secondary electrons signal) micrographs, respectively, of the etched cross-section of a thick flake having an average thickness of 130 μm. Lamellar precipitates of Sb_2Te_3, indicated by the arrows in Figure 3(c), are revealed to be randomly dispersed in the $AgSbTe_2$ matrix, whereas other parts of the matrix are free of precipitates, thereby suppressing formation of the interconnected Widmanstätten microstructure macroscopically across the entire sample. Overall, the density of precipitates appearing in the thick rapidly-cooled specimens is lower than that of the precipitates in the as-quenched master alloy.

Figure 4 shows a SEM (secondary electrons signal) micrograph of the etched cross-section of a thin flake (with thickness of about 60 μm). In this case, there is no evidence for formation of precipitates in an interconnected Widmanstätten pattern, and the microstructure is characterized by columnar grains with a width less than 5 μm.

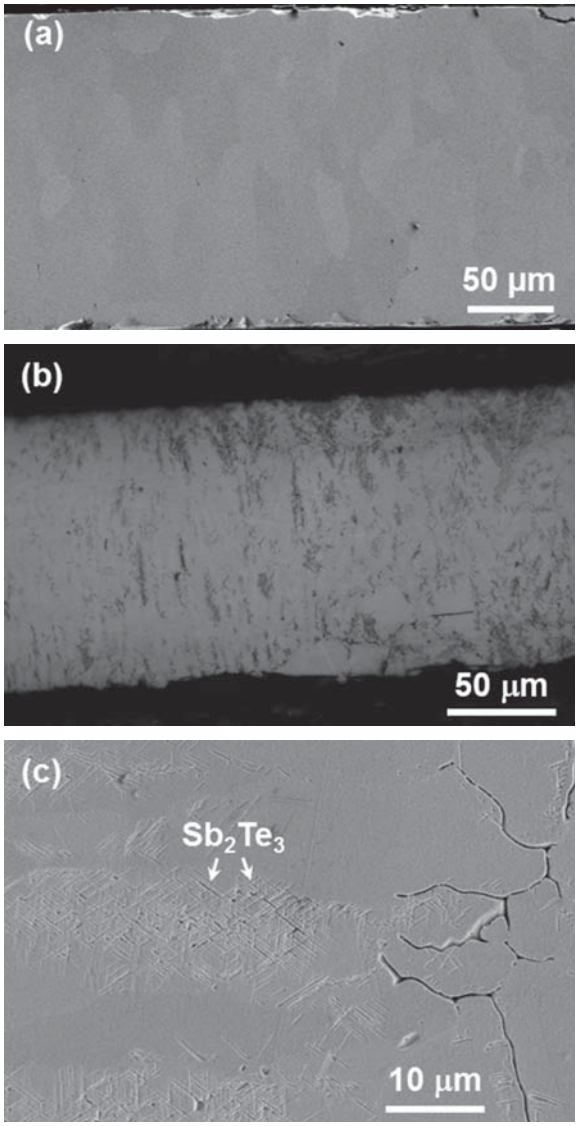

Figure 3. (a) Secondary electron micrograph of the non-etched cross section of a rapidly solidified thick flake (thickness 130 μm). (b) Optical micrograph of the etched cross section of a rapidly solidified thick flake (thickness 130 μm). (c) Secondary electron micrograph of the etched cross section of a rapidly solidified thick flake (thickness 130 μm): the arrows indicate the Sb_2Te_3 precipitates.

The absence of Sb_2Te_3 precipitates (at least on the micrometric length scale) in the thin flake specimens indicates that δ-$AgSbTe_2$ phase was successfully quenched to form a single phase state, avoiding the undesirable precipitation of the Sb_2Te_3 phase above 360 °C. In this manner, we manage to obtain a supersaturated metastable single δ-$AgSbTe_2$ phase, which exhibits the largest lattice parameter, 6.0781 Å, in agreement with the values reported in literature,[13, 27] whereas lattice parameter gradually decreases with the increase of lattice equilibrium level as indicated in Table II. The latter is directly associated to

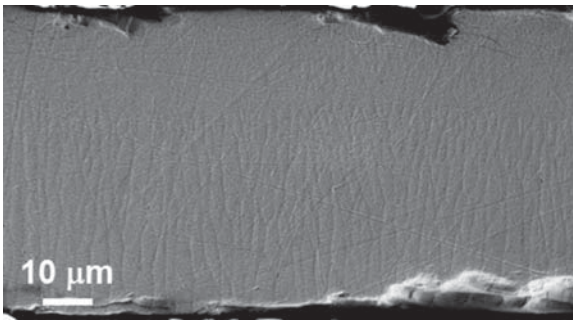

Figure 4. Secondary electron micrograph of the etched cross section of a rapidly solidified thin flake (thickness 60 μm).

the ongoing process of precipitation of the Sb_2Te_3-phase, leaving behind non-saturated δ-matrix. This effect is less marked for the thick flakes where partial precipitation of Sb_2Te_3 occurred, leading to a slightly lower value of the lattice parameter (6.0768 Å); this is due to the moderate cooling rates attained for the thick specimens, as opposed to the very fast cooling rate attained for the thin specimens. In the case of the master alloy, the cooling conditions are found to be the most moderate, accompanied by relatively high nucleation rate of the Sb_2Te_3 phase, leading to the lowest value of the lattice parameter (6.0752 Å).

We elucidate the faster cooling rates obtained for the thin specimens with respects to those of the thick specimens by means of thermal diffusion path, X, so that

$$X \approx \sqrt{\frac{\kappa}{C_p} t} \tag{3}$$

where κ, C_p and t are thermal conductivity, volumetric heat capacity and time. We associate t^{-1} to the average cooling rate of the specimens. We estimate the ratio κ/C_p, which is defined as *thermal diffusivity*, to be ca. 0.5 mm^2/s.[1] It is, therefore, estimated that the cooling rates of the thick and thin specimens are ca. $17 \cdot 10^3$ and $70 \cdot 10^3$ °C/s, respectively, assuming a temperature difference of 500 °C. For comparison, the cooling rate of the reference materials (12.5 mm dia. ingots) is estimated to be ca. 80 °C/s based on Eq. (3), which is significantly lower than that of the rapidly-solidified samples.

Figures 5(a and b) show the DSC traces (25 K/min) upon heating of the as cast reference sample, the as quenched rapidly solidified samples (representative of both thin and thick flakes) and the sintered rapidly solidified samples. According to the equilibrium phase diagram,[5] upon heating, we would expect the following sequence of endothermic events for our alloy:

$$145°C : \text{m-}Ag_2Te \rightarrow \text{c-}Ag_2Te \tag{4}$$

$$360°C : \text{c-}Ag_2Te + Sb_2Te_3 \rightarrow \delta\text{-}AgSbTe_2 \tag{5}$$

$$530°C : \delta\text{-}AgSbTe_2 + Sb_2Te_3 \rightarrow \delta\text{-}AgSbTe_2 \tag{6}$$

$$560°C : \delta\text{-}AgSbTe_2 \rightarrow \delta\text{-}AgSbTe_2 + \text{liquid} \tag{7}$$

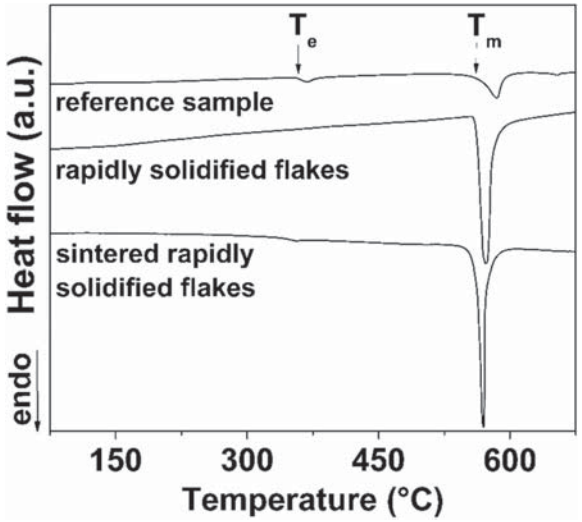

Figure 5. DSC signals upon heating at 25 K/min collected for the as quenched reference samples, the as quenched rapidly solidified flakes and the sintered rapidly solidified flakes.

None of the three samples shows the polymorphic transformation between monoclinic and cubic Ag_2Te at 145 °C, indicating that no monoclinic Ag_2Te formed upon cooling during the different sample processing routes. Subsequently, both the as cast reference sample and the sintered rapidly solidified flakes show an endothermic peak at 360 °C, T_e, which is absent in the as quenched rapidly solidified samples. The signal at 360 °C can be associated to the eutectoid reaction between cubic Ag_2Te and Sb_2Te_3 into δ-$AgSbTe_2$. The concomitant absence of the peak at 145 °C and the presence of the peak at 360 °C suggests the presence of a small amount of cubic Ag_2Te in the as cast reference sample and the sintered rapidly solidified flakes, that cannot be detected by XRD and metallographic analysis. The presence of cubic Ag_2Te in these two samples indicates that the cooling rate during sample processing was high enough to bypass the equilibrium polymorphic transformation at 145 °C, freezing this phase down to room temperature. Conversely, in the case of the rapidly solidified flakes, the absence of the endothermic peak at 360 °C suggests the no cubic Ag_2Te formed upon cooling because of the higher cooling rate, which inhibited the eutectoid decomposition of δ-$AgSbTe_2$.

Finally, all the samples start melting around 560 °C, T_m, in accordance with the equilibrium phase diagram.

An additional information from the DSC results is the effect of sintering on the microstructural evolution of the rapidly solidified flakes. The sintered sample obtained from the rapidly solidified flakes show the endothermic peak at 360 °C, which is absent in the as quenched rapidly solidified flakes, suggesting a partial decomposition of δ-$AgSbTe_2$ into cubic Ag_2Te and Sb_2Te_3 due to the moderate cooling rate after the sintering process.

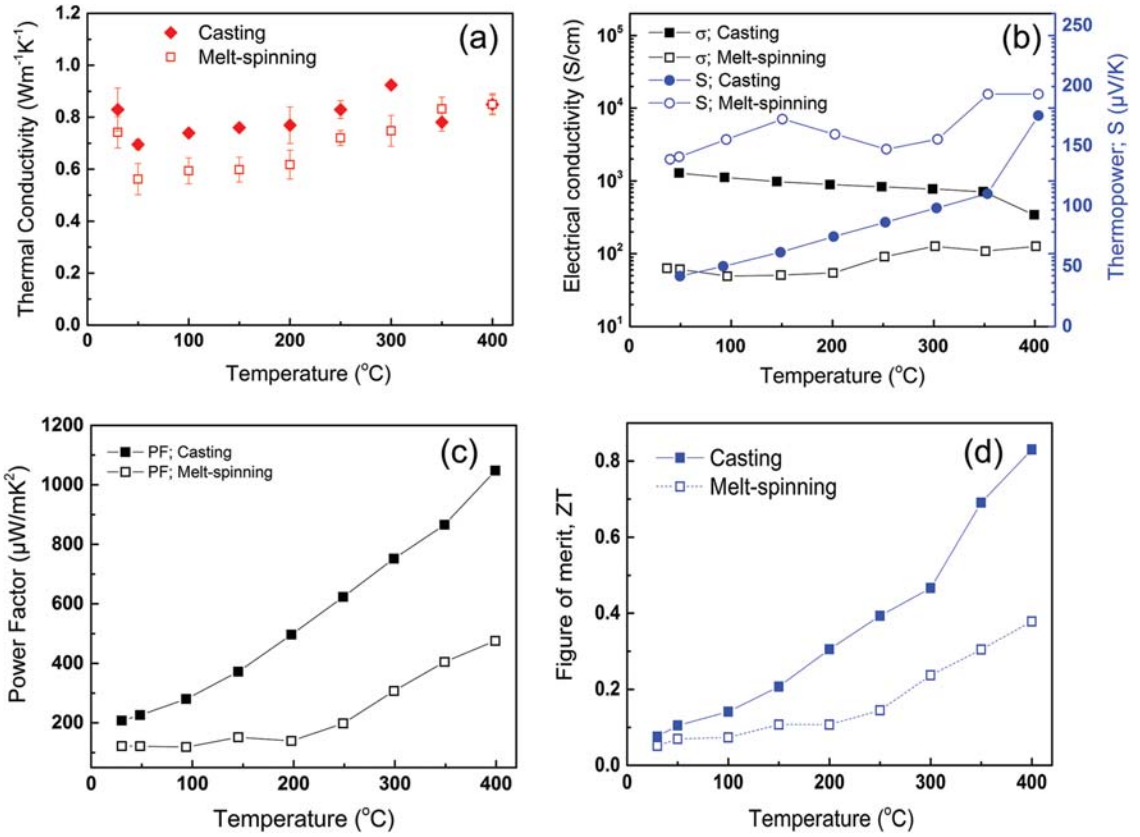

Figure 6. Temperature dependence of thermal conductivity (a), electrical conductivity and TE thermopower (Seebeck coefficient) (b), TE power factor (c), and TE figure of merit (d), measured for the reference samples (filled markers) and sintered rapidly solidified flakes (empty markers), labelled as "casting" and "melt-spinning," respectively.

To test the effects of rapid solidification on thermoelectric performance we measure thermal conductivity, electrical conductivity, and Seebeck coefficients for different temperatures ranging from 30 to 400 °C. The results for the reference samples and sintered samples obtained from rapidly-solidified flakes appear in Figures 6(a and b), and are referred to as "casting" and "melt-spinning," respectively. It is indicated in Figure 6(a) that thermal conductivity values of the rapidly-solidified specimens are generally lower than those of the reference materials. This can be associated to the finer grain size of the rapidly-solidified material (at the micrometer length scale) compared to that of the reference materials (dozens of micrometers), as well as to the supersaturated highly non-equilibrium lattice obtained after rapid solidification. These two factors, namely small grain size and lattice distortion, act as sources of phonon scattering, thereby reducing lattice thermal conductivity.[28–30] It is noteworthy that at 350 °C both datasets coincide, probably because both sample evolved towards the same equilibrium state above the eutectoid reaction (i.e., coexistence of Sb_2Te_3 and δ-phase), in agreement with DSC results shown in Figure 5. A similar trend is observed for the electrical conductivity datasets, Figure 6(b), where the values of the rapidly-solidified specimens are generally lower than those of the reference materials. This can also be associated to electron scattering,[31] although point defect scattering is much more dominant than grain boundary scattering. Since rapid solidification initiates electron scattering predominantly, it also contributes to increasing Seebeck coefficient values, as shown in Figure 6(b).

To combine the positive effect of rapid solidification on Seebeck coefficient with its negative effect on electrical conductivity, we calculate the resulting TE power factor, $PF \equiv \sigma \cdot S^2$.[32] Both PF values of the rapidly-solidified and reference samples are displayed in Figure 6(c). It is shown that the PF values obtained after rapid solidification are yet inferior to those of the reference materials. The positive effect of reduced thermal conductivity attained for the rapidly-solidified materials is balanced with the power factor, and the resulting TE *figure of merit*, $ZT \equiv PF \cdot T/\kappa$,[32] is displayed in Figure 6(d). The resulting figure of merit of the rapidly-solidified materials are lower than those of the reference materials. We associate this difference to the deleterious influence of super-saturated, distorted δ-matrix on electrical conductivity. Mitigation of this influence can

be further achieved by controlled annealing heat treatments that partially relax the matrix strain level.

4. CONCLUSIONS

In this work, the effects of rapid solidification on phase formation and microstructure evolution of an $Ag_{16.7}Sb_{30}Te_{53.3}$ compound were studied.

The equilibrium solid state precipitation of Sb_2Te_3 is progressively inhibited as the cooling rate increases, avoiding the formation of the typical Widmanstätten pattern which cause deterioration of the TE performances. Thus, a metastable supersaturated δ-$AgSbTe_2$ phase is obtained in rapidly solidified flakes. Microstructure refinement occurs upon rapid solidification with formation of columnar grains with thickness of about 5 μm and 10–30 μm in thin and thick flakes, respectively. After sintering of the as quenched rapidly solidified flakes, the DSC trace reveals a similar behavior to the one shown by the reference samples, indicating a partial decomposition of the non-equilibrium δ-$AgSbTe_2$ into the stable phases (i.e., cubic-Ag_2Te and Sb_2Te_3).

The formation of a highly supersaturated and distorted δ-matrix by rapid solidification causes both positive and negative effects on TE transport properties. It is concluded that rapid solidification yields reduced values of thermal conductivity and increased values of Seebeck coefficients; both are desirable for enhanced TE performance. On the other hand, it significantly reduces electrical conductivity, which negatively affects TE performance. We suggest that good compromise between these competing effects can be further achieved by controlled annealing heat treatments that partially relax the matrix strain level. Also, further investigations are needed to optimize the parameters of the rapid solidification process in order to maximize the cooling rate and obtain homogeneous single phase batches.

Acknowledgments: Yaron Amouyal wishes to acknowledge generous support from the Israel Science Foundation (ISF), Grant No. 698/13.

References and Notes

1. Y. Amouyal, *J. Electron. Mater.* 43, 3772 (**2014**).
2. D. T. Morelli, V. Jovovic, and J. P. Heremans, *Phys. Rev. Lett.* 101, 035901 (**2008**).
3. K. F. Hsu, S. Loo, F. Guo, W. Chen, J. S. Dyck, C. Uher, T. Hogan, E. K. Polychroniadis, and M. G. Kanatzidis, *Science* 303, 818 (**2004**).
4. M. D. Nielsen, C. M. Jaworski, and J. P. Heremans, *AIP Adv.* 5, 053602 (**2015**).
5. R. Schmid-Fetzer, Silver-Antimony-Tellurium Ternary Diagram, Handbook of Ternary Alloy Phase Diagrams edited by P. Villars, A. Prince, and H. Okamoto, ASM International, Materials Park, OH (**1995**).
6. H.-J. Wu and S.-W. Chen, *Acta Mater.* 59, 6463 (**2011**).
7. B. Du, Y. Yan, and X. Tang, *J. Electron. Mater.* 44, 2118 (**2015**).
8. P. A. Sharma, J. D. Sugar, and D. L. Medlin, *J. Appl. Phys.* 107, 113716 (**2010**).
9. B. Du, H. Li, J. Xu, X. Tang, and C. Uher, *J. Solid State Chem.* 184, 109 (**2011**).
10. D. T. Morelli, V. Jovovic, and J. P. Heremans, *Phys. Rev. Lett.* 101, 035901 (**2008**).
11. J. Ma, O. Delaire, A. F. May, C. E. Carlton, M. A. McGuire, L. H. VanBebber, D. L. Abernathy, G. Ehlers, T. Hong, A. Huq, W. Tian, V. M. Keppens, Y. Shao-Horn, and B. C. Sales, *Nature Nanotech.* 8, 445 (**2013**).
12. T. Su, X. Jia, H. Ma, C. Zang, L. Zhou, J. Guo, and N. Dong, *Mater. Lett.* 62, 3269 (**2008**).
13. S. N. Zhang, T. J. Zhu, S. H. Yang, C. Yu, and X. B. Zhao, *Acta Mater.* 58, 4160 (**2010**).
14. S. N. Zhang, T. J. Zhu, S. H. Yang, C. Yu, and X. B. Zhao, *J. Alloys Compd.* 499, 215 (**2010**).
15. M. H. Lee, K.-R. Kim, J.-S. Rhyee, S.-D. Park, and G. J. Snyder, *J. Mater. Chem. C* 3, 10494 (**2015**).
16. D. L. Medlin and J. D. Sugar, *Scripta Mater.* 62, 379 (**2010**).
17. R. W. Armostrong, J. W. Faust, and W. A. Tiller, Jr., *J. Appl. Phys.* 31, 1954 (**1960**).
18. B. Du, J. Xu, W. Zhang, and X. Tang, *J. Electron. Mater.* 40, 1249 (**2011**).
19. A. J. B. Vincent, B. P. Bewlay, B. Cantor, R. J. Zabala, R. P. La Force, S. C. Huang, and L. A. Johnson, *J. Mater. Sci. Lett.* 6, 121 (**1987**).
20. R. A. Young, The Rietveld method, Oxford University Press, New York (**1993**).
21. http://www.ing.unitn.it/~maud/index.html.
22. F. K. Lotgering, *J. Inorg. Nucl. Chem.* 9, 113 (**1959**).
23. A. Graff and Y. Amouyal, *J. Electron. Mater.* 45, 1508 (**2016**).
24. J. De Boor, C. Stiewe, P. Ziolkowski, T. Dasgupta, G. Karpinski, E. Lenz, F. Edler, and E. Mueller, *J. Electron. Mater.* 42, 1711 (**2013**).
25. F. Edler and E. Lenz, *AIP Conf. Proc.* 1449, 369 (**2012**),
26. D. M. Rowe (ed.), Thermoelectrics Handbook: Macro to Nano, CRC Press, Taylor and Francis Group, Broken Sound Parkway NW, Boca Raton, FL (**2006**).
27. S. Geller, *Acta Crystall.* 12, 46 (**1959**).
28. P. G. Klemens, *Proc. Phys. Soc. A* 68, 1113 (**1955**).
29. P. G. Klemens, *Phys. Rev.* 119, 507 (**1960**).
30. S.-H. Lo, J. He, K. Biswas, M. G. Kanatzidis, and V. P. Dravid, *Adv. Funct. Mater.* 22, 5175 (**2012**).
31. J. De Boor, T. Dasgupta, H. Kolb, C. Compere, K. Kelm, and E. Mueller, *Acta Mater.* 77, 68 (**2014**).
32. T. M. Tritt, *Ann. Rev. Mater. Res.* 41, 433 (**2011**).

Received: 8 April 2016. Accepted: 16 June 2016.